Gyrokinetic analysis of linear microinstabilities for the stellarator Wendelstein 7-X

P. Xanthopoulos
Max-Planck-Institut für Plasmaphysik, Teilinstitut Greifswald, Wendelsteinstrasse 1, D-17491 Greifswald, Germany

F. Jenko
Max-Planck-Institut für Plasmaphysik, Boltzmannstrasse 2, D-85748 Garching, Germany

(Received 27 September 2006; accepted 2 February 2007; published online 10 April 2007)

A linear collisionless gyrokinetic investigation of ion temperature gradient (ITG) modes—considering both adiabatic and full electron dynamics—and trapped electron modes (TEMs) is presented for the stellarator Wendelstein 7-X (W7-X) [G. Grieger *et al.*, *Plasma Physics and Controlled Nuclear Fusion Research 1990* (International Atomic Energy Agency, Vienna, 1991), Vol. 3, p. 525]. The study of ITG modes reveals that in W7-X, microinstabilities of distinct character coexist. The effect of changes in the density gradient and temperature ratio is discussed. Substantial differences with respect to the axisymmetric geometry appear in W7-X, concerning the relative separation of regions with a large fraction of helically trapped particles and those of pronounced bad curvature. For both ITG modes and TEMs, the dependence of their linear growth rates on the background gradients is studied along with their parallel mode structure. © *2007 American Institute of Physics*. [DOI: 10.1063/1.2714328]

I. INTRODUCTION

Over the past few years, the concept of optimized stellarators has revitalized the investigation of linear microinstabilities[1] in the core region of fusion plasmas. The effective suppression of neoclassical losses due to the special design of the magnetic geometry is expected to render the ion temperature gradient (ITG) mode[2] an important, if not dominant, transport mechanism. In addition to this, the trapped electron mode (TEM)[3] should also be taken into account, especially when ITG modes are either stable or only weakly unstable. The abundance of both analytical and numerical studies focusing on axisymmetric geometries sets a firm background for the understanding of microinstabilities in stellarators. Indeed, their generation is usually attributed to the free energy associated with temperature and density gradients and, therefore, constitutes a common factor for both tokamaks and stellarators. On the other hand, there was early evidence[4] that the geometrical aspects, which by and large distinguish the two configurations, are expected to lead to new features. The importance of geometry for the (linear) properties of the microinstabilities has been systematically verified, also in the context of nonaxisymmetric devices alone.[5]

It is reasonable and common to divide the existing works into two major categories, namely global (full torus) and local (flux tube) approaches. The former method has been used, in particular, to determine the spatial structure of unstable modes and to extract valuable information concerning the effect of important geometrical factors such as normal curvature and local shear.[6,7] However, as the ratio between the ion gyroradius and the system size becomes smaller, such global results are known to converge to the local ones (see, e.g., Ref. 8). Moreover, local approaches are able to reproduce the main findings of global simulations (see, e.g., Refs. 9–12) and, additionally, they are more suitable for performing large parameter scans (effect of temperature and density gradients, temperature ratio, etc.), mainly thanks to their relative efficiency. The present work falls into this category, with the exception that, instead of utilizing Boozer or Hamada coordinates in the context of the ballooning representation,[13] the flux tube is based on generalized Clebsch coordinates that have been described in a recent publication.[14] Here, the three-dimensional vacuum ($\beta=0$) equilibrium hs5v10u (see, e.g., Ref. 15) for the stellarator Wendelstein 7-X (W7-X) is employed (for finite β equilibrium studies, see Refs. 16 and 17).

The paper is organized as follows. In Sec. II, we address some basic geometrical issues. In particular, we describe the method to create a flux coordinate system based on Clebsch-type coordinates. In this context, a key characteristic of the W7-X configuration, as compared to an axisymmetric device, is demonstrated, namely the favorable interplay between bad curvature and magnetic trapping (see also the discussion in Ref. 5). In Sec. III, we present the gyrokinetic set of equations—upon which our computations are based—formulated as an initial-value problem (as opposed to an eigenvalue formulation; see, e.g., Refs. 10 and 11). This system is, in principle, able to handle generic toroidal geometries and also treat the nonlinear $\mathbf{E}\times\mathbf{B}$ advection (turbulence). At present, however, we restrict to the linear, collisionless version of the model and to closed flux surfaces. We also note that both passing and trapped particle effects are included (as in Refs. 5 and 10). Finally, in Sec. IV, we present the simulation results for the various cases under consideration. At this point, we would like to emphasize two major points stemming from the forthcoming analysis:

- The optimized stellarator geometry does *not* alter the basic characteristics of the microinstabilities and their dependencies on the principal physical parameters (temperature and density gradients, temperature ratio) as compared to a large aspect ratio tokamak.
- The geometrical aspects *do* differentiate between the two configurations, since the stellarator admits the coexistence of ITG modes of distinct character and the destabilizing effect of trapped electron dynamics is weaker as compared to a large aspect ratio tokamak.

II. GEOMETRICAL ASPECTS

In the present section, we describe the main characteristics of the magnetic configurations that will be considered throughout this study, namely the stellarator W7-X and a large aspect ratio tokamak with circular flux surfaces, in the context of the flux tube approach. This concept implies that all relevant geometrical information (metric tensor, Jacobian, etc.) is solely functions of the parallel coordinate. According to our method, these elements are constructed using field-aligned Clebsch-type coordinates (v_1, v_2, τ), which are numerically generated based on a realistic magnetic field equilibrium (for details, see Ref. 14). Here, v_1 and v_2 designate a selected magnetic field line, whereas τ is the coordinate following the magnetic field (in the sense that the vector $\mathbf{e}_\tau$ is parallel to the magnetic field $\mathbf{B}$). The advantage of this realization is twofold. First, the representation of the geometry is self-contained, since no transformation of coordinates (e.g., from VMEC[18] to Boozer) is required. Rather, the Clebsch coordinates are calculated directly via field line tracing. Second, and most important, these coordinates provide the possibility to investigate also "pathological" magnetic regions such as magnetic islands and ergodic layers. At present, however, only closed flux surfaces are treated and therefore the present work bears similarity to existing local treatments. [We mention in passing that this geometrical representation has been successfully benchmarked against analytical expressions for the $\hat{s}$-α model (see Ref. 14).]

In the case of closed, nested flux surfaces, it is always favorable to build up a flux coordinate system for which one coordinate (usually v_1) plays the role of the flux label. For the present implementation, this is achieved for a field line starting from the midplane (where it holds $B_r=0$). Note, however, that it is always possible to extract a flux coordinate system starting from an arbitrary point on the poloidal plane, as long as the initial conditions of the tracing algorithm guarantee that the contravariant vector ∇v^1 is normal to the flux surface at the starting point of the tracing (see also the discussion in Ref. 14).

For the complex magnetic configuration of a stellarator, it is useful to provide some numerical evidence supporting the construction of the flux coordinate system. Specifically, starting with the assumption that the coordinate v_1 has the property of a flux label, we calculate the vectors perpendicular to ∇v_1 along the field line. In case this family of vectors constitutes the tangent bundle of the manifold generated by the orbit of the line, one can claim that ∇v_1 is indeed normal to the surface traced by the field line and, therefore, v^1 is a flux label. To put this idea into practice, we first trace the magnetic line starting from the point with coordinates $(r,z)=(6,0)$ m (shown in Fig. 1) in the poloidal plane $\phi=0$. In Fig. 2 (left), we present the outcome of the tracing with step $\delta\phi=0.2\pi$. Given the fact that the W7-X stellarator has a period of 0.4π (fivefold symmetry), two poloidal planes are revealed, namely the "triangular" and the "bean-shaped" planes. Then, on the right of the same figure, we plot the (dimensionless) vectors $(\partial_z v^1, -\partial_r v^1)$, which are perpendicular to ∇v^1, and notice that they reproduce the tangent bundle, in view of the isomorphic structure to the orbit. This means that a flux coordinate system is indeed generated. For comparison, in the next case, we start the tracing from the point $(r,z)=(6,0.2)$ m which lies outside the midplane. It is clearly depicted that this change leads to incompatibility with the previous initial conditions, so that it is no longer possible to reproduce a flux coordinate system. Of course, ∇v^1 is by construction always perpendicular to the magnetic field, but this time *not* normal to the traced flux surface. Finally, we also note that the above results hold equally well for the tokamak geometry, even though for this simple case one can always resort to analytical reasoning.

We continue by focusing on the differences, with respect to geometry, between the simple tokamak case and the W7-X stellarator. This discussion will shed light on the linear properties of the microinstabilities for the two configurations. As is well known, the excitation of linearly unstable modes relies heavily on two key factors, namely magnetic trapping and bad curvature. For the stellarator, particles are mainly trapped in helical ripples, not on the outboard side like in an axisymmetric configuration. Indeed, besides the well-known banana-like trajectories, yet another class of trapped particles exists, namely those that are localized within a single helical field period.[19] Concerning curvature, one can characterize favorable regions for the development of microinstabilities through the sign and magnitude of the toroidal drift frequency,

$$\omega_d = \frac{cT_{i0}}{eB^3}\mathbf{B}\times\nabla B\cdot\mathbf{k}_\perp, \tag{1}$$

where T_{i0} is the background ion temperature (considered constant) and $\mathbf{k}_\perp$ denotes the wave vector that lies in the plane perpendicular to the magnetic field (in our formulation, this plane is spanned by the vectors ∇v_1 and ∇v_2).

It is commonplace that in the tokamak case, this quantity attains positive values on the outboard side, thus identifying this as a "bad curvature" region, which is favorable for the development of linearly unstable modes. For a stellarator configuration, things are more complicated, however. In Fig. 3, we plot the equivalent of ω_d according to our formulation, namely $-\mathcal{K}_2$ [see Eq. (6) below] along the field line. As usual, positive values indicate linearly destabilizing regions in which the modes are likely to be excited. It is instructive to combine this piece of information with the knowledge about regions of significant helical trapping. For the W7-X stellarator, an interesting observation is that the deeper magnetic wells are located in the middle of the flux tube (corre-

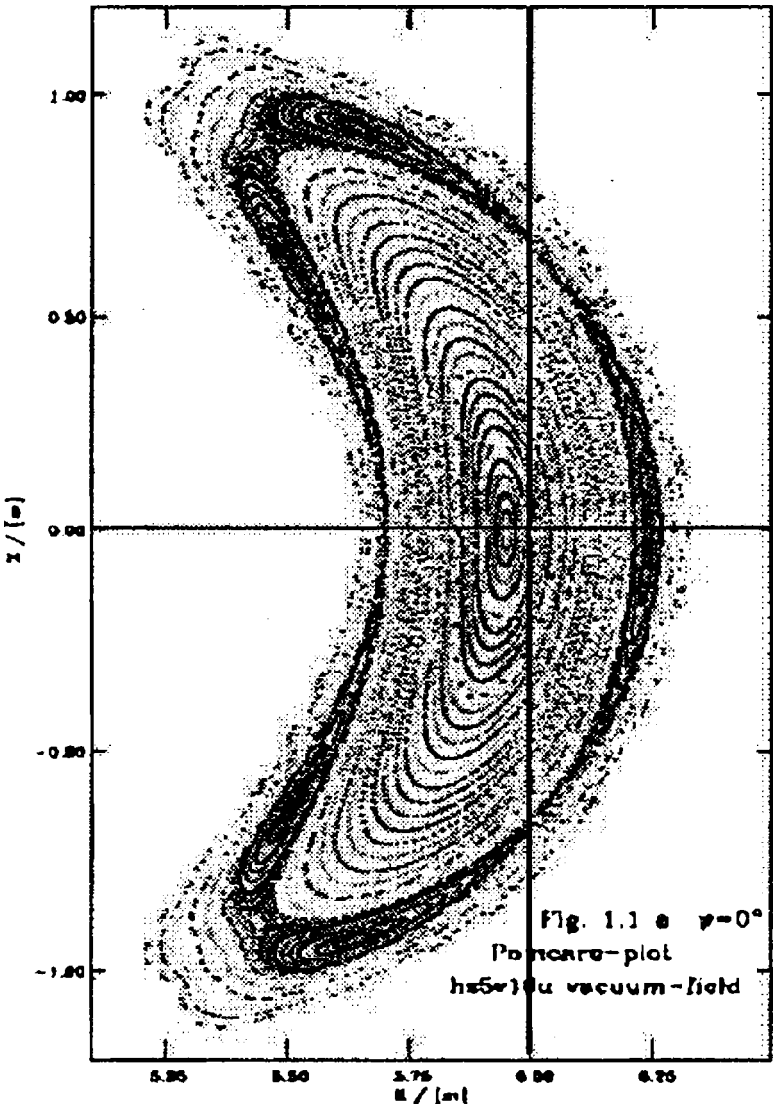

FIG. 1. Starting point of the traced flux tube for the present study.

sponding to the inboard side of the device), i.e., there is little overlap with regions of larger bad curvature (located mainly on the outboard side). Such behavior is in stark contrast to typical tokamak configurations, where the trapping and bad curvature regions almost coincide on the outboard side. This difference will play a central role in the discussion of ITG modes and TEMs later on.

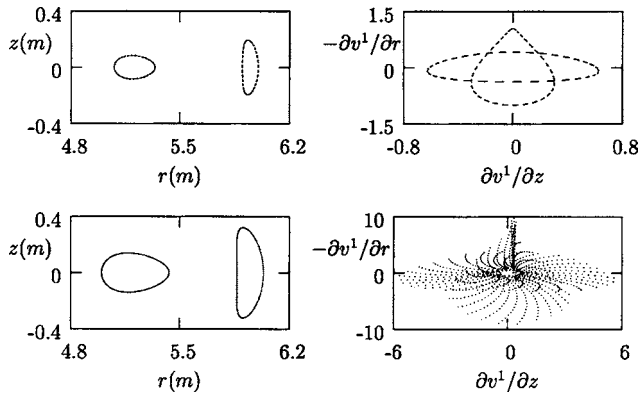

FIG. 2. (Top) Cross sections of the "triangular" and the "bean-shaped" planes starting from the symmetry plane (left) with isomorphic tangent space (right). (Bottom) Tracing starting outside the symmetry plane fails to reproduce a flux coordinate system (for the previous initial conditions).

III. PHYSICAL MODEL

In order to perform our simulations, we employ the linear version of the gyrokinetic turbulence code GENE.[20,21] This code, based on the standard gyrokinetic ordering (see, e.g., Ref. 22), was recently extended to handle generic toroidal geometries. Here, we briefly outline the system of equations (for more details, the reader is referred to Ref. 14).

A. The gyrokinetic Vlasov equation

The independent and dependent variables are normalized, respectively, according to Tables I and II (as velocity space coordinates, we use the parallel velocity $v_\parallel$ and the magnetic moment μ). The auxiliary quantities are the ion sound scale $\rho_s=c_s/\Omega_i$, the ion Larmor frequency $\Omega_i=eB_{\mathrm{ref}}/m_i c$, the ion sound speed $c_s=\sqrt{T_{\mathrm{e}0}/m_{\mathrm{i}}}$, the thermal velocity $v_{Tj}=\sqrt{2T_{j0}/m_j}$ of species j ($j=\mathrm{e},\mathrm{i}$), the safety factor q, a typical perpendicular equilibrium scale length $L_\perp$, and a

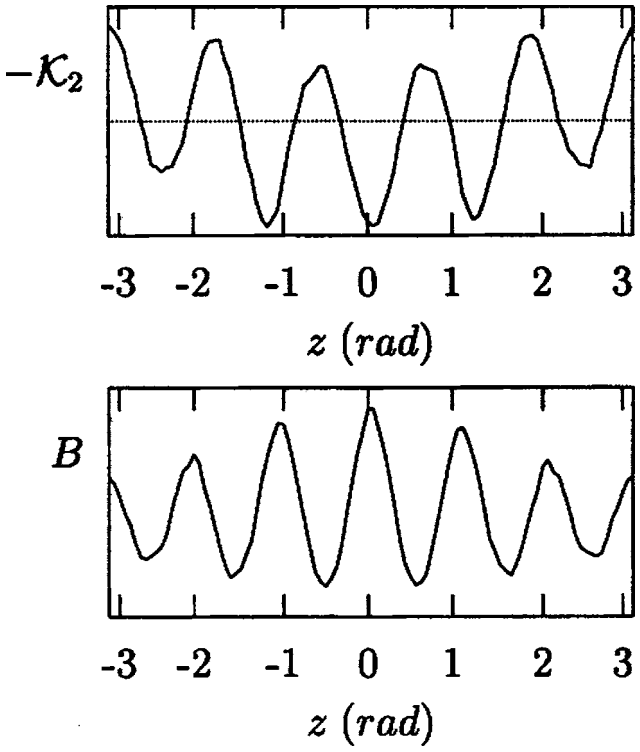

FIG. 3. (Top) The curvature profile for the W7-X flux tube characterizes the destabilizing regions (positive values). (Bottom) The magnetic field structure depicts the trapping effect. It is clear that regions with larger curvature are out of phase with the deeper magnetic wells. Here, z denotes the poloidal angle, which coincides with the parallel coordinate.

characteristic length R_{ref}. The latter is set usually equal to the major radius, but in principle it can be chosen arbitrarily, as long as it is used consistently everywhere. The magnetic field is normalized with respect to the quantity $B_{\mathrm{ref}}=JB^{\phi}$, where J is the Jacobian of the Clebsch system.

In vector form, the (normalized) gyrokinetic Vlasov equation for the perturbed part F_{j1} of the distribution function F_j then reads

$$\frac{\partial g_j}{\partial t} - \left[\boldsymbol{\omega}_n + \boldsymbol{\omega}_{T_j}\left(v_\parallel^2 + \mu B - \frac{3}{2}\right)\right] F_{j0}\cdot \mathbf{b}\times\frac{\nabla\chi_j}{B} + \mathbf{b}\times\frac{\nabla\chi_j}{B}\cdot\nabla G_j + \frac{1}{\sigma_j}(\mu B + 2v_\parallel^2)\mathbf{b}\times\frac{\nabla B}{B^2}\cdot\nabla G_j + \alpha_j v_\parallel \nabla_\parallel G_j - \frac{\alpha_j}{2}\mu\nabla_\parallel B\frac{\partial F_j}{\partial v_\parallel} = 0, \tag{2}$$

where we have used the definitions (gyroaveraged quantities are denoted by overbars)

$$g_j = F_{j1} + \sigma_j\alpha_j v_\parallel F_{j0}\hat{\epsilon}\beta_e\bar{A}_{1\parallel}, \quad G_j = g_j + \sigma_j\chi_j F_{j0},$$

TABLE I. Normalization of the independent variables.

t	$x_\perp$	$x_\parallel$	$v_\parallel$	μ
$L_\perp/c_s$	ρ_s	qR_{ref}	v_{Tj}	T_{j0}/B_{ref}

TABLE II. Normalization of the dependent variables.

F_{j0}	F_{j1}	Φ	$A_\parallel$
n_0/v_{Tj}^3	$(n_0/v_{Tj}^3)\rho_s/L_\perp$	$(T_{e0}/e)\rho_s/L_\perp$	$(qR_{\mathrm{ref}}\rho_s B_{\mathrm{ref}}\beta_e/L_\perp)\rho_s/L_\perp$

$$\chi_j = \bar{\Phi}_1 - \alpha_j v_\parallel\hat{\epsilon}\beta_e\bar{A}_{1\parallel}$$

as well as

$$\sigma_j = \frac{e_j}{e}\frac{T_{e0}}{T_{j0}}, \quad \alpha_j = \frac{v_{Tj}}{c_s}\frac{L_\perp}{qR_{\mathrm{ref}}},$$

$$\hat{\epsilon} = \left(\frac{qR_{\mathrm{ref}}}{L_\perp}\right)^2, \quad \beta_e = \frac{4\pi n_0 T_{e0}}{B_{\mathrm{ref}}^2},$$

$$\boldsymbol{\omega}_n = (\mathbf{bb}-\mathbf{I})\cdot\frac{\nabla n}{n}, \quad \boldsymbol{\omega}_{T_j} = (\mathbf{bb}-\mathbf{I})\cdot\frac{\nabla T_j}{T_j}.$$

As equilibrium distribution we assume a Maxwellian which, in normalized units, reads

$$F_{j0}(v_\parallel,\mu) = \pi^{-3/2}e^{-(v_\parallel^2+\mu B)}.$$

In the Clebsch coordinates (v^1,v^2,z), the gyrokinetic Vlasov equation takes the form

$$\frac{\partial g_j}{\partial t} + \left(\frac{\partial\chi_j}{\partial v^1}\frac{\partial G_j}{\partial v^2} - \frac{\partial\chi_j}{\partial v^2}\frac{\partial G_j}{\partial v^1}\right) + F_{j0}\left[\omega_{n,1} + \omega_{T_j,1}\left(v_\parallel^2 + \mu B - \frac{3}{2}\right)\right]\frac{\partial\chi_j}{\partial v^2} - \frac{\mathcal{M}\hat{b}^3}{B}F_{j0}\left[\omega_{n,2} + \omega_{T_j,2}\left(v_\parallel^2 + \mu B - \frac{3}{2}\right)\right]\frac{\partial\chi_j}{\partial v^1} + \frac{1}{2\sigma_j}(\mu B + 2v_\parallel^2)\left(\mathcal{K}_1\frac{\partial G_j}{\partial v^1} + \mathcal{K}_2\frac{\partial G_j}{\partial v^2}\right) + \alpha_j v_\parallel\hat{b}^3\frac{\partial G_j}{\partial z} - \frac{\alpha_j}{2}\mu\hat{b}^3\frac{\partial B}{\partial z}\frac{\partial F_j}{\partial v_\parallel} = 0, \tag{3}$$

where

$$\mathcal{M} = \hat{J}[g^{11}g^{22} - (g^{12})^2], \quad \hat{J} = J/R_{\mathrm{ref}}, \quad \hat{b}^3 = R_{\mathrm{ref}}b^3 \tag{4}$$

and

$$\omega_{n,k} = -\frac{L_\perp}{n}\frac{\partial n}{\partial v^k}, \quad \omega_{T_j,k} = -\frac{L_\perp}{T_j}\frac{\partial T_j}{\partial v^k} \quad (k=1,2). \tag{5}$$

In addition, the curvature operators read

$$\mathcal{K}_1 = -c_v\frac{R_{\mathrm{ref}}}{B}\frac{\partial B}{\partial v^2}, \quad \mathcal{K}_2 = c_v\frac{R_{\mathrm{ref}}}{B}\frac{\partial B}{\partial v^1}, \quad c_v = \frac{2L_\perp}{R_{\mathrm{ref}}}. \tag{6}$$

Note that in Eqs. (5) and (6), v^1 and v^2 are *not* normalized, and therefore the prefactors $L_\perp$ and R_{ref} enter the equations. This is in contrast to Eq. (3), where v^1 and v^2 are dimensionless. We also notice that, in view of the specific choice for B_{ref}, the contravariant element reads

$$\hat{b}^3 = \frac{1}{\hat{J}B}. \tag{7}$$

In summary, the magnetic geometry enters the gyrokinetic Vlasov equation essentially in three ways—through the magnetic field strength B, the Jacobian J, and the magnetic curvature terms $\mathcal{K}_1$ and $\mathcal{K}_2$. In the framework of a flux tube approach, all of these quantities are solely functions of the parallel coordinate z.

B. The gyrokinetic field equations

The self-consistent electromagnetic field is determined via the gyrokinetic Poisson equation

$$\sum_j e_j \sigma_j [1 - \Gamma_0(b_j)]\Phi = \sum_j \pi e_j B \int d\mu dv_\parallel J_0(\lambda_j) g_j \tag{8}$$

and the gyrokinetic Ampère's law

$$\left(\nabla_\perp^2 - \frac{1}{2}\hat{\epsilon}\beta_e \sum_j \sigma_j \alpha_j^2 \frac{e_j}{e}\Gamma_0(b_j)\right) A_\parallel = -\sum_j \pi \alpha_j \frac{e_j}{e} B \int d\mu dv_\parallel J_0(\lambda_j) v_\parallel g_j. \tag{9}$$

Here, the Bessel function J_0 and the function $\Gamma_0(b_j) = e^{-b_j} I_0(b_j)$ (where I_0 is the modified Bessel function) have been introduced. The arguments λ_j and b_j are defined, respectively, as

$$b_j = -\frac{T_j}{T_e}\frac{m_j}{m_i}\frac{e^2}{e_j^2}\frac{1}{B^2}\nabla_\perp^2, \quad \lambda_j^2 = 2\mu B b_j. \tag{10}$$

The magnetic geometry enters these equations through the perpendicular Laplacian, which, according to the flux tube method, reads

$$\nabla_\perp^2 A = \sum_{i,j=1}^{2} g^{ij}\partial_i \partial_j A. \tag{11}$$

In summary, the magnetic geometry enters the gyrokinetic field equations through the magnetic field strength B and the elements g^{11}, g^{12}, and g^{22} of the metric tensor.

C. Phase space resolution

For the W7-X simulations, the following points have to be taken into account:

- The W7-X configuration belongs to the Helias (helically advanced stellarator) family, aiming at improving the reactor prospects of a classical stellarator. It is designed as a five field period configuration with rotational transform close to unity and practically zero global shear. The latter property enables us to reduce the number of points in the radial direction down to $N_x = 4$. Actually, increasing the number of radial points by a factor of 2 causes insignificant changes to the growth rates and the parallel mode structure. In contrast, for the finite shear tokamak case, where the radial resolution is important, we typically set $N_x = 16$.

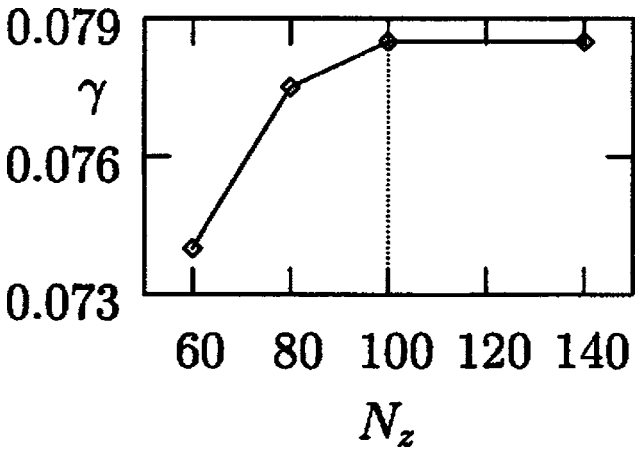

FIG. 4. Convergence test for the W7-X flux tube simulation: Linear growth rate as a function of the number of parallel grid points. The vertical line indicates a (rough) minimum value to ensure the reliability of the simulations.

- The metric elements for W7-X are helically modulated along the parallel direction. This fact imposes a significant increase in the number of parallel points as compared to the tokamak case. In order to specify the minimum number that at the same time guarantees reliable results, we performed a convergence test, gradually raising the number of parallel points—while keeping the length of the flux tube fixed—until the growth rate saturates (see Fig. 4 for a standard case). It turned out that it is necessary to use $N_z = 100$ points, while for the tokamak case, it is sufficient to employ only $N_z = 16$.
- For completeness, we also provide information about the velocity space and time resolution in these calculations. In $(v_\parallel, \mu)$ space, we find it sufficient to employ (32,8) points. This amounts to a total of 256 velocity space points. A doubling of any of these two numbers has no significant impact. The time step is always adjusted according to the parallel Courant condition imposed by the numerical scheme. Since the latter is always much smaller than the inverse frequency (and linear growth rate) of the microinstabilities under consideration, time step convergence is not an issue.

IV. RESULTS AND DISCUSSION

In the following, we present numerical results for various sets of physical parameters. The flux tube considered is produced by field line tracing, starting from the initial point $(r, z, \phi) = (6, 0, 0)$ m on the outboard side of the device. The reason for this particular choice is twofold: First, the initial point should be chosen such that it leads to a flux coordinate system and, second, the field line should be close to the axis to assure good MHD equilibrium data and to allow for a reasonable comparison with the $\hat{s}$-α case. Other than that, this flux tube is not special by any standards. The resulting geometrical input data for the GENE simulations are presented in Ref. 14. Since W7-X has a fivefold discrete symmetry, all geometric coefficients are periodic after one poloidal turn, and it is sufficient to track the field line (only) that far.

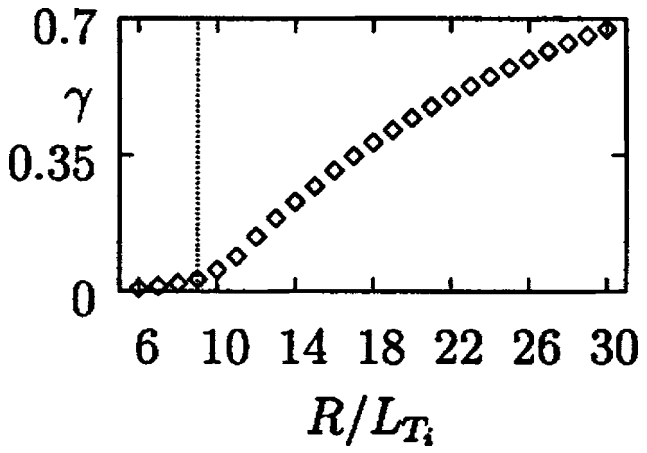

FIG. 5. Linear growth rates of the ITG mode with adiabatic electrons for the W7-X stellarator. The vertical line designates the transition from the trapped ion to the toroidal ITG regime. Here, $\eta=\infty$ and $\tau=1$.

Our goal in this section is to provide qualitative arguments as well as concrete quantitative output concerning the linear characteristics of the microinstabilities. The investigation of linear growth rates, real frequencies, and, in addition, of the parallel mode structure of the fluctuations will provide useful information in this context. Moreover, we will make systematic parameter studies with respect to the temperature and density gradients and the ion-to-electron temperature ratio. Through this effort, we aim at providing insight into the linear physics of various drift-type instabilities for the W7-X configuration.

A. ITG modes with adiabatic electrons

Starting with the simplest scenario, we examine the linear properties of the ITG driven mode assuming adiabatic electrons. First, we investigate the dependence of the linear growth rate (normalized, here and thereafter, with respect to c_s/R) on the normalized ion temperature gradient R/L_{T_i} (here, R denotes the radial position of the starting point for the field-line tracing, i.e., $R=6$ m). In Fig. 5, we present the results of linear GENE simulations, considering a flat density profile so that $\eta_i \equiv L_n/L_{T_i} \rightarrow \infty$. We also assume equal temperatures for ions and electrons, i.e., $\tau \equiv T_{i0}/T_{e0}=1$. Note that, throughout the present study, the magnitude of the perpendicular wave number is set equal to $k_\perp \rho_i=0.3$ for both the stellarator and the axisymmetric configurations. This nominal value represents a plausible choice, in view of existing global studies for W7-X (see, e.g., Ref. 6) as well as various turbulence simulations in tokamak geometry (see, e.g., Ref. 21).

In Fig. 5, it is easy to discern two separate branches with respect to the slope of the curve (this characteristic is also true for the growth curves appearing in Refs. 11 and 17). The latter is relatively small up to $R/L_{T_i}<9$. This part of the curve corresponds to the so-called trapped ion mode,[23] as will be shown shortly. For larger values of R/L_{T_i}, toroidal (bad curvature) effects start to dominate, and the linear growth rate increases substantially. We note that in a standard tokamak case, there exists a smooth transition from a toroidal ITG mode to a trapped ion mode in the *long wavelength limit* for fixed R/L_{T_i} (see, e.g., Ref. 24). A distinct property of the W7-X configuration is, therefore, the coexistence of the two modes.

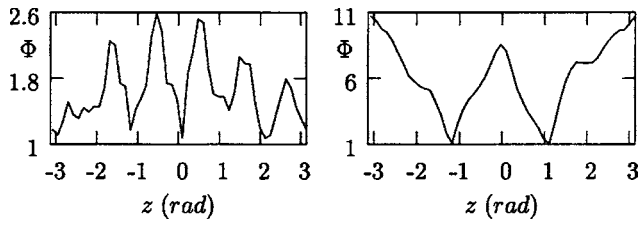

FIG. 6. Parallel mode structure of the potential fluctuations for the trapped ion mode (left) and the toroidal ITG mode (right), revealing different localization patterns. The fact that the amplitudes are not small at the end of the flux tube is due to the periodicity of the geometric coefficients and zero global shear.

In order to support the identification of the microinstability at low values of R/L_{T_i} as a trapped ion mode, we present the parallel mode structure of the (absolute value of) potential fluctuations in Fig. 6. In particular, two values of R/L_{T_i} are considered, namely $R/L_{T_i}=7$ and 15, corresponding to the two distinct regions of the $\gamma(R/L_{T_i})$ curve. The difference is evident in terms of the pattern of the perturbations. In the latter case, the mode is clearly localized in the regions of bad curvature (compare with Fig. 3), whereas in the first case this is not true. On the contrary, the fluctuations are mainly situated in the magnetic trapping regions and, in fact, the magnitude of the perturbations is proportional to the depth of the magnetic wells.

The relative simplicity of the present case allows for an analytical treatment based on a reduced (gyro)fluid model (see, e.g., Ref. 25). This approach successfully describes the linear growth rates for large values of the ion temperature gradient, thus providing an estimate for the "effective" critical gradient $(R/L_{T_i})_{\text{crit}}$ of the toroidal branch. According to such a simple model, the latter is expected to scale as

$$\gamma \propto \frac{c_s}{\sqrt{RL_{T_i}}}\left[\frac{R/L_{T_i}-(R/L_{T_i})_{\text{crit}}}{R/L_{T_i}}\right] \tag{12}$$

at fixed $k_\perp \rho_i$. This estimate is verified for the W7-X case in Fig. 7. Indeed, the fit of the toroidal branch of the linear

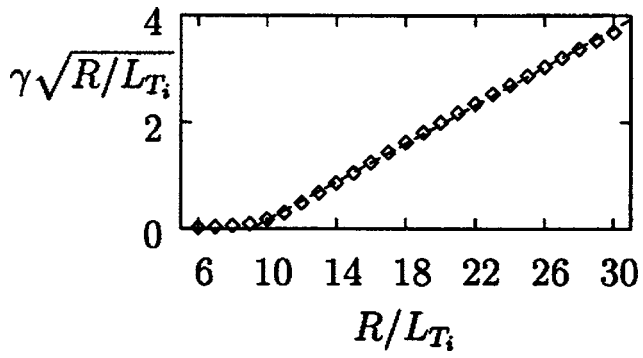

FIG. 7. The rescaled linear growth rate of the toroidal ITG mode is well described by the fit curve $\gamma\sqrt{R/L_{T_i}} \propto [R/L_{T_i}-(R/L_{T_i})_{\text{crit}}]$ (dashed line), which provides the effective critical gradient: $(R/L_{T_i})_{\text{crit}}=9.1$.

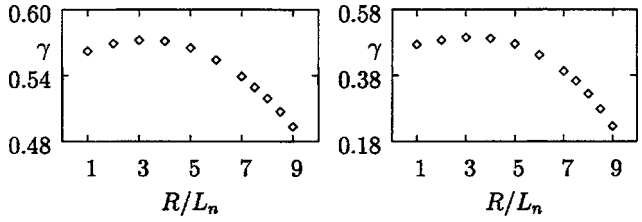

FIG. 8. (Left) Growth rates of the ITG mode with adiabatic electrons for the W7-X configuration with varying R/L_n. The ion temperature gradient is fixed to the value $R/L_{T_i}=24$. (Right) Growth rates for the tokamak configuration with $R/L_{T_i}=10$. For both cases the temperature ratio is $\tau=1$.

growth rate curve to the above expression is excellent. By means of this procedure, it is thus possible to extract the effective critical value for the ion temperature gradient. It is given by $(R/L_{T_i})_{\mathrm{crit}}=9.1$. Obviously, at such large values of the normalized ion temperature gradient, the magnetic geometry has only little effect on the properties of the toroidal ITG instability, and the behavior of the W7-X stellarator resembles that of a usual tokamak.

1. Effect of density gradient

So far, the analysis employing adiabatic electrons has been performed assuming a flat density profile. Now we wish to investigate the effect of a finite η_i on the development of the ITG mode. For this, we set up the following case for the W7-X configuration, suitable for direct comparison with the axisymmetric geometry. The ion temperature gradient is fixed to the value $R/L_{T_i}=24$ (well inside the toroidal branch of the growth rate curve) while the density gradient and, therefore, the η_i value is varied. In addition, we assume equal ion and electron temperatures. As shown in Fig. 8, an increase in R/L_n is at first destabilizing. This trend is reversed, however, for larger values of the density gradient. It is interesting to note that this kind of behavior is not peculiar to the stellarator configuration but, on the contrary, it has also been encountered in linear gyrokinetic simulations for tokamaks (see, e.g., Ref. 25). For concreteness, we perform a similar study for the $\hat{s}$-α tokamak geometry, using the so-called Cyclone base case parameters[26] (this setup is used for our tokamak simulations hereafter). Clearly, one can conclude that the effect of the density gradient on the linear growth rate is qualitatively the same in both geometries.

In Fig. 9, we present two ITG growth rate curves for the W7-X configuration. These curves correspond to identical parameters, except for the value of the density gradient: While one curve corresponds to a flat density profile, the other corresponds to $R/L_n=5$. It is interesting to note that, for relatively small temperature gradients, the density gradient has a stabilizing effect, in agreement with existing threshold analyses (see, e.g., Ref. 27). Nevertheless, well inside the toroidal branch, we notice a crossing of the two curves. Therefore, one may infer that the final effect of the density gradient is a destabilization of the mode. Once again, the swapping of stability trends is also present in tokamak studies.[28]

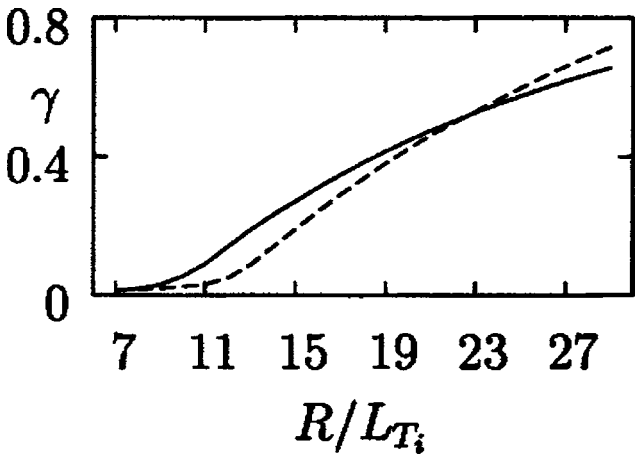

FIG. 9. Linear growth rate curves of ITG modes with adiabatic electrons for the W7-X configuration in the flat density profile limit (solid line) and for $R/L_n=5$ (dashed line).

2. Effect of temperature ratio

Next, we address the question of how the temperature ratio $\tau=T_{i0}/T_{e0}$ affects the growth rate of the ITG mode for the W7-X configuration and compare the results with those obtained in the simple tokamak geometry. It turns out that again no qualitative difference is observed between the two configurations. This statement is justified by Fig. 10, where we plot the linear growth rates for W7-X as a function of τ for $R/L_{T_i}=15$. The density profile is considered flat. We deliberately focus on the range $\tau=(0,1]$, which includes the case $T_e \gg T_i$, a quite interesting scenario in view of the often employed electron cyclotron resonance heating method. For direct comparison, we also present the curve corresponding to the tokamak configuration, for $R/L_{T_i}=7$. It is seen that the impact of temperature ratio is qualitatively the same for both configurations. Specifically, as the electron temperature starts to exceed the ion temperature, a destabilization occurs, which is subsequently reversed.

Further, we examine two W7-X cases bearing identical characteristics with the exception of the temperature ratio, namely $\tau=1$ and 0.5. The corresponding growth rate curves are depicted in Fig. 11. For moderate values of the ion temperature gradient, the smaller temperature ratio destabilizes the mode. In particular, the effective critical temperature gradient for the $\tau=0.5$ case is smaller (~ 8) than the value for the $\tau=1$ case (~ 9). From this point on, the two curves evolve according to Eq. (12) and, eventually, they cross each other. Therefore, as R/L_{T_i} becomes larger, the trend changes

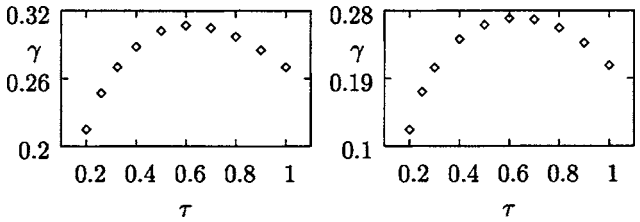

FIG. 10. Growth rates of the ITG mode with adiabatic electrons for the W7-X configuration (left) and the tokamak configuration (right) with varying τ. The density profile is considered flat.

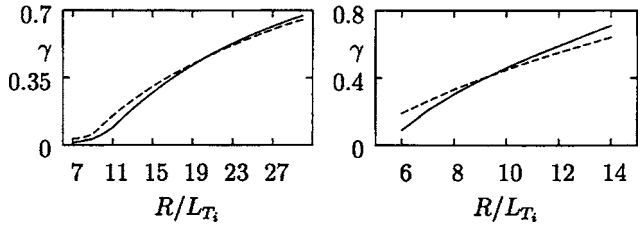

FIG. 11. Growth rate curves of the ITG mode with adiabatic electrons for W7-X (left) and tokamak configurations (right) for the cases $\tau=0.5$ (dashed line) and $\tau=1$ (solid line). The characteristic crossing takes place irrespective of the geometry.

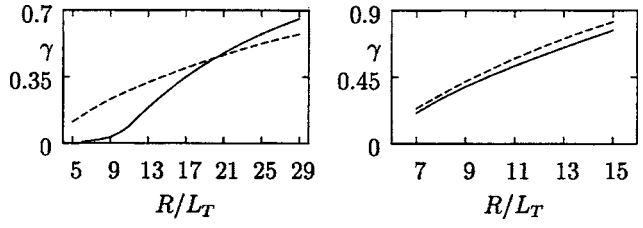

FIG. 12. Comparison between temperature gradient driven TEM (dashed line) and ITG mode with adiabatic electrons (solid line) for the W7-X configuration (left) and the simple tokamak geometry (right). For both modes, the density profile is considered flat and $\tau=1$. In the stellarator case, the TEM threshold is $(R/L_{T_e})_{\mathrm{crit}}=3.2$.

and we have a stabilizing effect. In Ref. 11 it is stated that, for the W7-X stellarator, the small temperature ratio has a stabilizing effect. This conclusion is understandable, since in that study, R/L_{T_i} is quite large (around 30). Once again, this feature is not peculiar to the stellarator configuration, but it is quite a typical case for the tokamak, too. To support this, also shown in Fig. 11, are the growth rate curves corresponding to the $\hat{s}$-α tokamak geometry.

In summary, ITG modes with adiabatic electrons in the W7-X configuration exhibit a transition from trapped ion modes to toroidal ITG modes with increasing R/L_{T_i} but for a *fixed* $k_\perp\rho_i$. In the latter regime, both stellarator and tokamak configurations exhibit the same basic characteristics. In particular, no qualitative differences are observed with respect to the effects of the density gradient and the temperature ratio. These parameters can be either stabilizing or destabilizing, depending on the value of the normalized ion temperature gradient.

B. Analysis including full electron dynamics

In the present subsection, we will investigate the collisionless trapped electron mode (TEM) as well as the effects of nonadiabatic (both passing and trapped) electrons on the behavior of the ITG mode. To reduce the numerical cost, the ion-to-electron mass ratio is set to 400 in the TEM case (this has little effect, as can be inferred from Ref. 21) while it is set to 1836 in the ITG case. For the TEMs, we set the ion temperature gradient equal to zero, while we vary either the (normalized) electron temperature gradient R/L_{T_e} or the density gradient R/L_n. This scenario is by no means artificial since it corresponds to experiments with dominant central electron heating like those described in Refs. 29 and 30. For the ITG modes, we keep both ion and electron gradients nonzero, assuming a flat density profile. This setup refers to a combined instability that manifests itself either as a single mode, in the sense that the real frequency varies continuously with η, or as a collection of distinct modes, in case there is a wide frequency separation.[10]

1. Collisionless trapped electron mode

At first, we concentrate on the study of the collisionless trapped electron mode driven by electron temperature gradients. As will be shown, this mode—which is again connected to bad curvature effects—can be quite important in a variety of situations, e.g., for plasmas with dominant electron heating and/or low density, etc. Our purpose is to quantify the basic characteristics of these TEMs by means of various code diagnostics.

In the stellarator case, particle trapping is mainly due to helical ripples, and as discussed previously, regions of effective helical trapping (i.e., the deeper magnetic wells) may be efficiently separated from regions of larger bad curvature. This is the case for W7-X—in stark contrast to the tokamak case, in which the bulk of trapped electrons is located in the bad curvature region, i.e., on the outboard side. Based on this argument, one expects TEMs to be less pronounced for this stellarator configuration. This is indeed true, as depicted in Fig. 12. Here, the growth rates of both TEM and toroidal ITG mode with adiabatic electrons are shown for the two configurations (for both modes, a flat density profile is assumed).

In the tokamak case, the TEM growth rates lie systematically above the ITG ones, also with the tendency to deviate more as the temperature gradient increases. On the contrary, for the W7-X configuration, the TEM is rather pronounced for small temperature gradients. However, it is gradually attenuated and becomes less important than the ITG mode as the gradient is further increased. This behavior can be better comprehended through an inspection of the parallel mode structure of the fluctuating potential and perpendicular electron temperature (see Fig. 13). The former reflects the distribution of the trapped particles, in line with the structure of the magnetic field amplitude, as shown in Fig. 3. Indeed, the potential amplitudes follow exactly the effectiveness of the trapping, i.e., they tend to peak in regions where the magnetic wells are deeper. In addition, the amplitudes of the perpendicular temperature fluctuations,

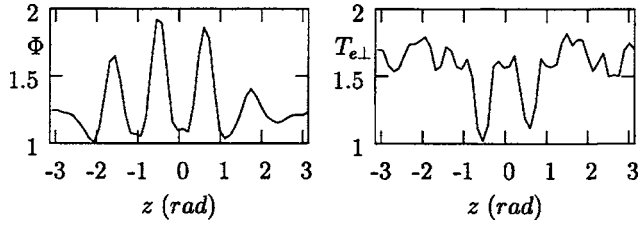

FIG. 13. Parallel mode structure for the fluctuating potential and perpendicular electron temperature of the TEM for W7-X. The favorable decoupling between regions with effective helical trapping (middle of flux tube) and larger bad curvature (ends of the tube) is clearly depicted. Here, $R/L_{T_e}=15$, the density profile is flat, and $\tau=1$.

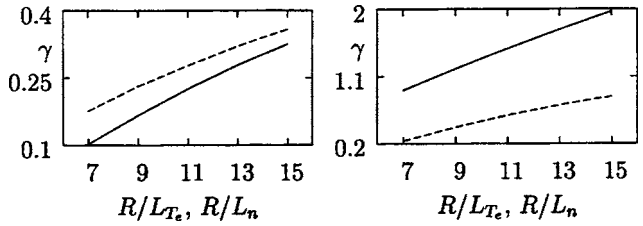

FIG. 14. Comparison between density (solid line) and temperature (dashed line) gradient driven TEM for the W7-X configuration (left) and the axisymmetric geometry (right).

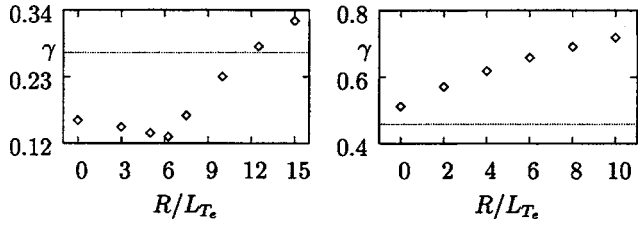

FIG. 15. (Left) Growth rates of the two species ITG mode for W7-X with fixed $R/L_{T_i}=15$. (Right) Same for simple tokamak geometry with fixed $R/L_{T_i}=10$. The dotted line shows the growth rate level of the ITG mode with adiabatic electrons for each case. Here, $\eta=\infty$ and $\tau=1$.

which are again mainly carried by the trapped particles, characterize the dynamics of the TEM. In particular, it is readily seen that the drive stems primarily from regions with pronounced bad curvature. Indeed, the amplitudes there obviously exceed those in the middle of the flux tube, where the bad curvature effect is not so acute. The overall picture now becomes clear: The favorable decoupling of larger bad curvature regions with the deeper trapping wells prevents the bulk of the helically trapped population to get destabilized and therefore the TEM effect is weaker in the stellarator case. However, we repeat that it is by no means negligible, especially for small values of the temperature gradient, as shown in Fig. 12 (left).

In order to complete the investigation of the TEM, we present results concerning this mode driven exclusively by the density gradient. For this, we explicitly set $R/L_{T_i}=R/L_{T_e}=0$ and vary R/L_n. In order to compare the two geometries, we juxtapose the growth rate curves for both temperature and density gradient driven TEMs (see Fig. 14). The discrepancy is evident since, for the stellarator configuration, the density gradient driven TEM is weaker relative to the temperature gradient driven one, a situation completely opposite to the tokamak geometry, where the former is clearly dominant. We also note that, as in the case of temperature gradient driven TEM, the mode propagates in the electron diamagnetic drift direction.

2. ITG mode including full electron dynamics

Here, we extend the investigation of the ITG mode that has been presented above by including full (trapped and passing) electron dynamics. This case turns out to be rather intricate. Indeed, the interaction of the two species, *both* driving the instability through their respective gradients, can give rise to various situations. Thus, depending on the specific parameters, one generally obtains microinstabilities of either a mixed ITG-TE nature or of pure ITG or TEM character. In order to identify specific modes, it is therefore useful to examine their real frequencies along with the parallel amplitudes of the fluctuations. Our aim is to study these features in the context of the W7-X configuration, as well as to highlight potential differences in comparison with the simple tokamak case.

To begin with, we address the question of how electron kinetics affects the ITG mode. For this, we choose a typical value for the ion temperature gradient, $R/L_{T_i}=15$ (on the toroidal branch, in order to facilitate the comparison with the axisymmetric case) and vary the electron temperature gradient, starting from zero up to $R/L_{T_e}=R/L_{T_i}$. The density profile is considered flat once again. The result for W7-X, as shown in Fig. 15, demonstrates that nonadiabatic electrons are in fact stabilizing (with respect to the adiabatic case) as long as the electron temperature gradient is not too large. Only when both temperature gradients become almost equal do we see a *mild* destabilization of the mode, a feature that is also reported in Ref. 5. In the same figure, we also present respective growth rate curves for the tokamak case, this time employing $R/L_{T_i}=10$. It is obvious that the behavior of the mode is totally different here, since the effect of nonadiabatic electrons is clearly destabilizing. Specifically, the growth rate for $R/L_{T_e}=R/L_{T_i}=10$ is about 1.5 times larger than the one for the ITG mode with adiabatic electrons. Moreover, cases have been reported in which the growth rate is even increased by a factor of 2–3.[24] For the W7-X case, the increase of the growth rate for $R/L_{T_e}=R/L_{T_i}=15$ only amounts to 18%.

We now concentrate on the ITG mode for the stellarator case, with the aim of further analyzing and understanding its behavior. As stated before, it is useful to calculate the corresponding real frequencies. In case a discontinuity is detected, this implies a transition between two different branches of microinstabilities. As shown in Fig. 16 (left), this is indeed observed for W7-X. The first branch is by definition an ITG mode, since it starts out with a zero electron temperature gradient (and the density profile is flat). However, it is characterized by a negative frequency, which, according to our convention, means that the mode propagates in the *electron* diamagnetic drift direction. It is interesting to note that such a branch is also encountered in axisymmetric configurations, but only in the *long wavelength limit*.[31]

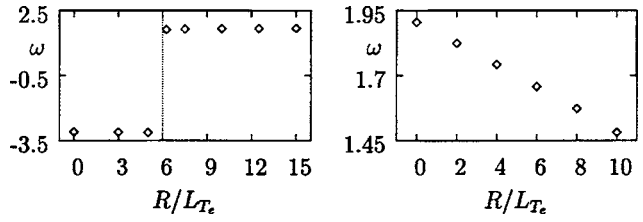

FIG. 16. Real frequencies of the two species ITG mode for the W7-X configuration (left) and the simple tokamak geometry (right), corresponding to Fig. 15. The vertical line designates the transition between the two ITG modes.

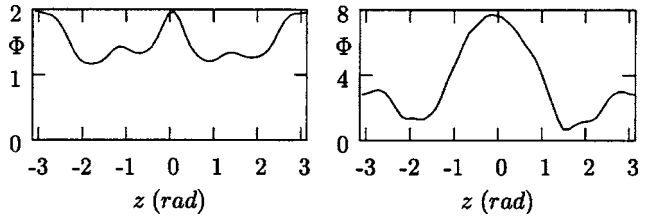

FIG. 17. Parallel mode structure of the fluctuating potential for the two species ITG mode. The temperature gradients read $R/L_{T_i}=15$, $R/L_{T_e}=3$ (left) and $R/L_{T_i}=15$, $R/L_{T_e}=15$ (right). Here, $\eta=\infty$ and $\tau=1$.

The second branch is quite difficult to characterize, since both species contribute to the drive over the whole range of the mode. However, we can still discern typical ITG characteristics, namely the mode propagates in the ion diamagnetic direction (whereas the TEMs presented previously always drift in the electron direction) and the quasilinear ion heat flux is always larger than the respective electron heat flux (see below). As an additional argument, the signatures of the $T_{e\perp}$ fluctuations clearly differ (for the same electron temperature gradient, $R/L_{T_e}=15$) in the pure TEM and the present mode [compare Figs. 13 (right) and 18 (right)]. In summary, the stellarator is characterized by the coexistence of ITG modes of distinct character, as in the adiabatic electron case. This is in contrast to the tokamak case also depicted in Fig. 16, where only the usual toroidal branch of the mode appears.

The two toroidal ITG branches differ significantly with respect to their parallel mode structure. The amplitude profiles of the fluctuating potential for the two modes are shown in Fig. 17. For the case with small electron temperature gradient, the potential fluctuations are relatively flat. This could be attributed to the fact that the fast passing electrons manage to "short-circuit" them and, consequently, the mode is stabilized. Furthermore, the amplitude profiles of $T_{e\perp}$, shown in Fig. 18, demonstrate enhanced trapped electron dynamics for the second branch, which outperforms the previous stabilizing effect resulting in the excitation of the mode.

It is also instructive to compute the ratio of the quasilinear ion and electron heat fluxes as a function of the electron temperature gradient. This quantity is shown in Fig. 19. It is evident that for small values of R/L_{T_e}, the two species are almost decoupled, in the sense that there is a great disparity between the two fluxes. For the second mode, these fluxes become almost equal (but the ion flux remains greater than the electron one). In this regime, one could also speak of a

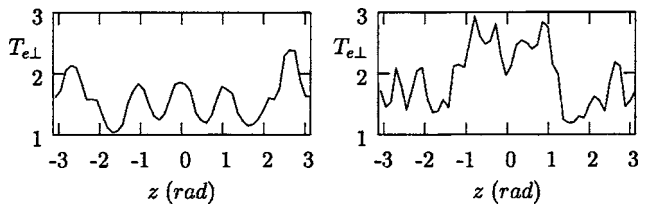

FIG. 18. Parallel mode structure of the fluctuating perpendicular electron temperature for the two species ITG mode. The temperature gradients read $R/L_{T_i}=15$, $R/L_{T_e}=3$ (left) and $R/L_{T_i}=15$, $R/L_{T_e}=15$ (right). Here, $\eta=\infty$ and $\tau=1$.

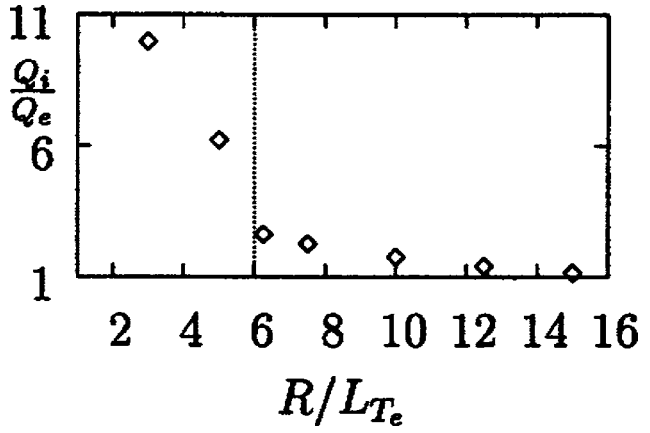

FIG. 19. Ratio of the quasilinear ion and electron heat fluxes as a function of the electron temperature gradient. Both channels get gradually coupled with increasing drive. The vertical line designates the transition between the two types of ITG modes.

"mixed" ITG-TE mode. In order to assess the contribution of the additional trapped electron drive to this mode, we determine its linear growth rate as a function of $R/L_T=R/L_{T_e}=R/L_{T_i}$, and compare with the respective mode in the adiabatic electron approximation (see Fig. 20). In the result for the W7-X configuration, we have deliberately included the point $R/L_T=12$, which does *not* correspond to the mixed mode. For this reason, we notice a jump in the growth rate curve. A promising feature of the W7-X configuration is that the gap between the two curves is much smaller than in the tokamak case.

V. CONCLUSIONS

In the present work, we have investigated the linear characteristics of two basic microinstabilities in the core plasma of the stellarator experiment W7-X, namely ITG modes and collisionless TEMs. To this aim, we have solved the linear gyrokinetic equations in appropriate Clebsch-type coordinates, using toroidal flux tubes. This study reveals a unique feature for the stellarator configuration, namely a *coexistence* of unstable ITG modes of distinct character. This statement holds true for both the adiabatic electron approximation and full electron dynamics.

For adiabatic ITG modes, one obtains an "effective" threshold $(R/L_{T_i})_{\text{crit}}$, below which the mode develops into a trapped ion mode with much smaller linear growth rates. In

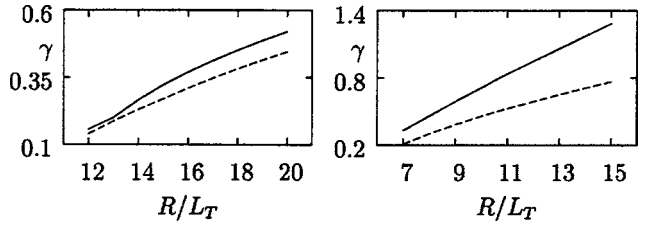

FIG. 20. Growth rate curves of the two species ITG mode for W7-X (left) and the simple tokamak geometry (right), for $R/L_{T_e}=R/L_{T_i}=R/L_T$. The solid line represents the two species mode, whereas the dashed line stands for the ITG mode with adiabatic electrons. Here, $\eta=\infty$ and $\tau=1$.

axisymmetric geometry, this latter branch only exists in the long wavelength limit. For large normalized ion temperature gradients, the bad curvature effects dominate, and the mode manifests the usual toroidal character that is well known from tokamak studies. This similarity even holds when one studies the effects of changes in the temperature ratio and density gradient. For small values of the temperature gradient, an increase of the electron temperature destabilizes the mode, whereas a finite density gradient has a stabilizing effect. However, depending on the parameters, "crossings" in the growth rate curves might occur that indicate a swapping of these trends. Therefore, it is not safe to predict lightheartedly the effect of these factors, but rather case-dependent studies are required.

Concerning the study of the ITG mode in the presence of nonadiabatic (both passing and trapped) electrons, we notice the existence of two separate branches for constant R/L_{T_i} and varying R/L_{T_e}. Both these modes bear ITG features but differ with respect to the electron dynamics. The first branch is dominated by the effect of passing electron dynamics, which actually stabilizes the mode. It drifts in the electron diamagnetic direction. The second branch, for large values of R/L_{T_e}, switches over to the ion drift direction and displays enhanced trapped electron dynamics. This results in a "mixed" mode, which eventually causes a further, if *moderate*, destabilization of the ITG mode compared to the adiabatic electron limit.

Substantial differences between the stellarator and tokamak configurations are revealed through the investigation of TEMs. We conclude that, for the W7-X case, the relative decoupling of regions with pronounced bad magnetic curvature and those with a large trapped fraction has a stabilizing effect on this mode. TEMs are thus expected to be weaker in W7-X as compared to a typical large aspect ratio tokamak. On the other hand, their linear growth rates are by no means negligible, and their critical gradients are relatively small. Thus, TEM turbulence can still play an important role in a device like W7-X. The decoupling mentioned above is not perfect and allows for significant TEM activity.

The present analysis should be considered as the groundwork for nonlinear gyrokinetic studies of core turbulence in W7-X as well as in other stellarator devices. Our setup is, in principle, even able to deal with the nonlinear dynamics inside magnetic islands and the ergodic layer. Progress in this direction will be documented in forthcoming publications.

ACKNOWLEDGMENTS

We would like to thank T. Dannert and F. Merz for help with the GENE code and R. Kleiber for useful discussions. In addition, one of the authors (P.X.) gratefully acknowledges funding from a Marie Curie Fellowship contract.

[1] P. C. Liewer, Nucl. Fusion **25**, 543 (1985).
[2] W. Horton, D. I. Choi, and W. M. Tang, Phys. Fluids **24**, 1077 (1981).
[3] B. Coppi and G. Rewoldt, Phys. Rev. Lett. **33**, 1329 (1974).
[4] A. Bhattacharjee, J. E. Sedlak, P. L. Similon, M. N. Rosenbluth, and D. W. Ross, Phys. Fluids **26**, 880 (1983).
[5] G. Rewoldt, L.-P. Ku, and W. M. Tang, Phys. Plasmas **12**, 102512 (2005).
[6] V. Kornilov, R. Kleiber, R. Hatzky, L. Villard, and G. Jost, Phys. Plasmas **11**, 3196 (2004).
[7] G. Jost, T. M. Tran, W. A. Cooper, L. Villard, and K. Appert, Phys. Plasmas **8**, 3321 (2001).
[8] J. Candy, R. E. Waltz, and W. Dorland, Phys. Plasmas **11**, L25 (2004).
[9] J. L. V. Lewandowski, Phys. Plasmas **10**, 4053 (2003).
[10] G. Rewoldt, L.-P. Ku, W. M. Tang, and W. A. Cooper, Phys. Plasmas **6**, 4705 (1999).
[11] T. Rafiq, R. Kleiber, M. Nadeem, and M. Persson, Phys. Plasmas **9**, 4929 (2002).
[12] A. Kendl and H. Wobig, Phys. Plasmas **6**, 4714 (1999).
[13] J. W. Connor, R. J. Hastie, and J. B. Taylor, Phys. Rev. Lett. **40**, 396 (1978).
[14] P. Xanthopoulos and F. Jenko, Phys. Plasmas **13**, 092301 (2006).
[15] X. Bonnin, A. Mutzke, C. Nührenberg, J. Nührenberg, and R. Schneider, Nucl. Fusion **45**, 22 (2005).
[16] V. Kornilov, R. Kleiber, and R. Hatzky, Nucl. Fusion **45**, 238 (2005).
[17] A. Kendl, Plasma Phys. Controlled Fusion **43**, 1559 (2001).
[18] P. Hirshman, U. Schwenn, and J. Nührenberg, J. Comput. Phys. **87**, 396 (1990).
[19] A. Gibson and J. B. Taylor, Phys. Fluids **10**, 2653 (1967).
[20] F. Jenko, W. Dorland, M. Kotschenreuther, and B. N. Rogers, Phys. Plasmas **7**, 1904 (2000).
[21] T. Dannert and F. Jenko, Phys. Plasmas **12**, 072309 (2005).
[22] T. S. Hahm, Phys. Fluids **31**, 2670 (1988).
[23] B. B. Kadomtsev and O. P. Pogutse, Nucl. Fusion **11**, 67 (1971).
[24] R. D. Sydora, V. K. Decyk, and J. M. Dawson, Plasma Phys. Controlled Fusion **38**, 281 (1996).
[25] M. A. Beer, Ph.D. thesis, Princeton (1995).
[26] A. M. Dimits, G. Bateman, M. A. Beer *et al.*, Phys. Plasmas **7**, 969 (2000).
[27] F. Jenko, W. Dorland, and G. W. Hammett, Phys. Plasmas **8**, 4096 (2001).
[28] F. Romanelli, Phys. Fluids B **1**, 1018 (1989).
[29] F. Ryter, G. Tardini, F. De Luca *et al.*, Nucl. Fusion **43**, 1396 (2003).
[30] X. Garbet, P. Mantica, F. Ryter *et al.*, Plasma Phys. Controlled Fusion **46**, 1351 (2004).
[31] L. Chen, S. Briguglio, and F. Romanelli, Phys. Fluids B **3**, 611 (1991).